IOP Publishing Phys. Med. Biol. 65 (2020) 015003 (15pp) https://doi.org/10.1088/1361-6560/ab563e

Physics in Medicine & Biology

IPEM Institute of Physics and Engineering in Medicine

PAPER

RECEIVED
1 July 2019

REVISED
28 October 2019

ACCEPTED FOR PUBLICATION
8 November 2019

PUBLISHED
10 January 2020

Optimizing 4D abdominal MRI: image denoising using an iterative back-projection approach

B Denis de Senneville[1,3], C R Cardiet[2], A J Trotier[2], E J Ribot[2], L Lafitte[1], L Facq[1] and S Miraux[2]

[1] 'Institut de Mathématiques de Bordeaux', University of Bordeaux/CNRS UMR 5251, 351 Cours de la Libération, 33405 Talence Cedex, France

[2] 'Centre de Résonance Magnétique des Systèmes Biologiques', University of Bordeaux/CNRS UMR 5536, 146 rue Léo Saignat 33076 Bordeaux Cedex, France

[3] Author to whom any correspondence should be addressed.

E-mail: bdenisde@math.u-bordeaux.fr

Keywords: 4D-MRI, abdominal MRI, denoising, iterative back-projection

Supplementary material for this article is available online

Abstract

4D-MRI is a promising tool for organ exploration, target delineation and treatment planning. Intra-scan motion artifacts may be greatly reduced by increasing the imaging frame rate. However, poor signal-to-noise ratios (SNR) are observed when increasing spatial and/or frame number per physiological cycle, in particular in the abdomen.

In the current work, the proposed 4D-MRI method favored spatial resolution, frame number, isotropic voxels and large field-of-view (FOV) during MR-acquisition. The consequential SNR penalty in the reconstructed data is addressed retrospectively using an iterative back-projection (IBP) algorithm. Practically, after computing individual spatial 3D deformations present in the images using a deformable image registration (DIR) algorithm, each 3D image is individually enhanced by fusing several successive frames in its local temporal neighborood, these latter being likely to cover common independent informations. A tuning parameter allows one to freely readjust the balance between temporal resolution and precision of the 4D-MRI.

The benefit of the method was quantitatively evaluated on the thorax of 6 mice under free breathing using a clinically acceptable duration. Improved 4D cardiac imaging was also shown in the heart of 1 mice. Obtained results are compared to theoretical expectations and discussed. The proposed implementation is easily parallelizable and optimized 4D-MRI could thereby be obtained with a clinically acceptable duration.

1. Introduction

Due to its superiority on soft-tissue contrast and its non-invasive feature, MRI is an established modality in clinical routine. In particular, it has become a promising technique for imaging moving organs at the abdomen or cardio-thoracic level with the possibility of obtaining time-resolved 3D images (4D-MRI). Many applications can be considered, such as lung exploration and detection of lung nodules (Ohno *et al* 2017, Feng *et al* 2019), cystic fibrosis (Dournes *et al* 2016), or, to an even more complex degree, 3D-cine cardiac imaging (Jahnke *et al* 2006). 4D-MRI is also a tool of choice for planning sessions in radiation (Paganelli *et al* 2015, Jinsoo *et al* 2017) and high intensity focused ultrasound (HIFU) (Ferrer *et al* 2019) therapies of abdominal tumors: it thereby facilitates the prospective analysis of organ localisation on the therapeutic treatment and allows monitoring changes in target motion patterns during the treatment course (Stemkens *et al* 2016).

A wide range of approaches have been developed to obtain 4D-MRI images. The data needs to be re-ordered retrospectively in 3D according to the respiratory or cardiac cycles. For this purpose, the most recent approaches use self-gating techniques where a motion signal is extracted from the acquired data (Trotier *et al* 2016, Han *et al* 2017, Higano *et al* 2017). Then, to construct high-resolution 4D-MR data, both prospective gated imaging and retrospective binning methods have been explored in previous studies (Tryggestad *et al* 2013, Liu *et al* 2015,

Stemkens *et al* 2015). For both prospective and retrospective binning, the challenge is to populate motion bins densely enough within an acceptable acquisition duration. Missing-data artefacts are frequenlty encountered and a large slice-thickness is generally mandatory to obtain sufficient field-of-view (FOV) and signal-to-noise ratio (SNR). These approaches are generally limited in spatial resolution, and super-resolution (SR) techniques have thus recently been proposed to compensate for large voxel sizes in acquired images (Van Reeth *et al* 2015, Chilla *et al* 2017, Freedman *et al* 2018): several low-resolution images containing independent information of the same region are fused using an iterative back-projection (IBP) to produce one high-resolution image. An intrinsic drawback of such SR-approaches is that it can not provide any additional information in image regions prone to unmoving tissues. Alternatively, sparse imaging has also been introduced and has enabled to obtain 5D cardiac information (3D images plus two distinct temporal dimensions representing cardiac and respiratory phases, respectively) with extension of XD-GRASP techniques (Feng *et al* 2018). These different techniques use specific k-space encoding, most often radial or spiral trajectories. These last methods are known to be more robust to motion. Further motion correction methods based on linear phase correction to all the acquired k-space have been introduced (Cheng *et al* 2012) and it can be coupled with acceleration technique to obtain free-breathing images in a wide range of applications (Cheng *et al* 2015, Zhang *et al* 2015, Chen *et al* 2017). In the latter approaches, the presence of movement due to breathing generates long acquisition times to obtain high spatial resolution images in 4D, preventing the use of this type of imaging in clinical routine. The complexity of reconstruction methods using self gating information, and/or compressed sensing reconstructions with multi-channel coils is also an issue that must be taken care of for the development of abdominal and cardiopulmonary MRI in clinical routine.

For all above-mentioned methods, multiple 2D or 3D images with sufficient SNR need to be acquired, which imposes several restrictions during MR-acquisition in terms of either: image FOV, spatial resolution, frame number, voxel sizes or acquisition duration. In the current paper, our approach is to put aside any SNR considerations during the MR-signal acquisition. A 4D-data set is acquired during the physiological motion cycle (breathing or cardiac) with a large FOV, privileged spatial resolution and frame number (thereby avoiding intra-scan motion artifacts, only inter-scan motion are present) and isotropic voxels. The consequential SNR penalty in reconstructed data is retrospectively addressed by adjusting the balance between temporal resolution and precision of the 4D-MRI, using an IBP strategy (Irani and Peleg 1993).

Our contribution is four-fold:

(i) An image-enhancement method is proposed to optimize 4D abdominal MRI: a 4D data set with a high spatio-temporal resolution is acquired during the physiological motion. Each 3D image are subsequently individually enhanced by fusing several successive frames—these latter being likely to contain common independent anatomical informations—using an IBP-strategy.
(ii) An input parameter—referred to as $\rho \in [0, 1]$ in the scope of this study—is introduced to freely adjust the balance between the precision (favored by increasing ρ toward 1) and the temporal resolution (favored by decreasing ρ toward 0) of the 4D output.
(iii) The performance of the proposed 4D image-enhancement method is quantitatively analysed in terms of both precision and accuracy in the thorax of 6 mice. Intrinsic limits of the method in the presence of complex organ deformations are illustrated in the heart of 1 mouse. Obtained results are compared to compressed sensing reconstructions and to theoretical expectations, and discussed.
(iv) The benefit of using multi-CPU, GPU (graphics processing unit) and computer cluster architectures is evaluated.

2. Materials and methods

2.1. Proposed retrospective 4D IBP-enhancement method

The proposed method (detailed in figure 1) consists of three successive steps:

- **Step #1—MR-acquisition/reconstruction:** A 4D-MRI with isotropic voxels and optimized spatial resolution/frame number is first acquired during the physiological motion cycle (i.e. breathing if the thorax is screened, cardiac cycle if it is the heart) (see section 2.1.1). In order to obtain each dynamic 3D image in a reduced scan time (thereby avoiding intra-scan motion artefacts), the amount of acquired data in the k-space has to be limited. This largely affects in turns the signal-to-noise ratio (SNR).
- **Step #2—Estimation of 3D organ deformations:** At this point, we have a set of low-SNR 4D data with optimized spatial resolution/frame number. 3D inter-scan spatial deformation present in the 3D images were individually estimated using a deformable image registration (DIR) algorithm (see section 2.1.2). Potential deformation perturbations in motion estimates induced by the presence of noise in input images were compensated.

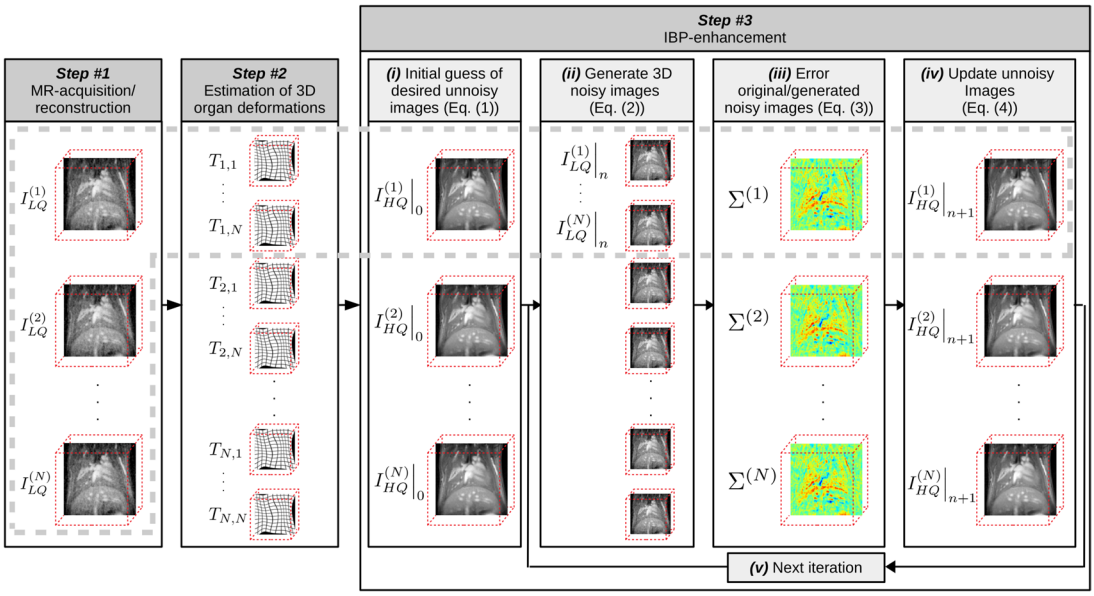

Figure 1. Data processing sequence designed for 4D abdominal MRI using the proposed IBP-algorithm. The dashed light-grey line encompasses data involved in the reconstruction of one single frame (here frame #1).

- **Step #3—IBP-enhancement:** Each 3D low-SNR image was individually enhanced by fusing several successive frames covering commmon informations using an IBP approach (Irani and Peleg 1993) (see section 2.1.3). Practically, we iteratively minimized differences between acquired 3D low-SNR images and images generated from back-registering a guess of the unnoisy image.

2.1.1. *Step #1: acquisition of 4D data with optimized spatial resolution/frame number*

A Self-Gated 3D UTE (ultrashort echo time) sequence was used, as described in section 2.2.2. For the rest of the manuscript, let N be the number of 3D noisy frames. We denote by $I_{LQ}^{(k)}$ the original 'low quality' (noisy) images (k is a time index, $k \in \{1, ..., N\}$). Assuming the periodicity of the breathing and cardiac activities, k is taken modulo N once it goes out the range $[0, N]$ in equations that follow.

2.1.2. *Step #2: estimation of 3D organ deformations*

$\forall (n, k) \in \{1, ..., N\}^2$, let $T_{n,k}$ be the 3D spatial transformation that allows registering the frame k (i.e. $I_{LQ}^{(k)}$, referred to as the 'moving image') onto the frame n (i.e. $I_{LQ}^{(n)}$, referred to as the 'reference image'). Both forward and backward non-rigid displacements (i.e. $T_{n,k}$ and $T_{n,k}^{-1}$) are mandatory for the achievement of Step #3. $T_{n,k}$ and $T_{n,k}^{-1}$ were estimated using a 3D optical flow (OF) algorithm (Zachiu *et al* 2015). Briefly, the OF-algorithm calculates non-rigid displacement between two imaging frames according to a transport equation, with an additional constraint on motion smoothness to model elastic organ deformation. An inverse consistency error (ICE), as defined by Christensen and Johnson (2001), was minimized in order to provide a pair of symmetric transformations $(T_{n,k}, T_{n,k}^{-1})$ for a given pair of frames indexed by (n, k).

At this point, it must be noticed that OF-estimates are inherently sensitive to the presence noise in OF-input (noisy) images. $\forall (n, k) \in \{1, ..., N\}^2$, the potential noise in forward transformations $T_{n,k}$ were reduced using the following two-steps process:

(i) Perturbations in $T_{n,k}$ arising from the presence of noise in 'moving images' (index k) could be easily reduced using a voxelwise temporal (along k) average-filter (kernel size $= 5$) applied on $T_{n,k}$, for each $n \in [1, ..., N]$ individually.

(ii) We could then take benefit of the assumption that $T_{n,n}$ has to be identically equal to 0 $\forall n \in [1, ..., N]$ (no organ motion): once filtered as done in (i), $T_{n,n}$ is filled by OF persistant biases arising from the presence of noise in the 'reference image' (index n). For any given n, $T_{n,n}$ thereby provides a voxelwise OF-bias map which was subtracted to $T_{n,k}$ $\forall k \in [1, ..., N]$ (practically: $T_{n,k} = T_{n,k} - T_{n,n}$, $\forall k \in [1, ..., N]$).

This two-steps process was performed for backward transformations $T_{n,k}^{-1}, \forall (n,k) \in \{1,...,N\}^2$, similarly.

2.1.3. Step #3: IBP image enhancement

We denote by $I_{HQ}^{(k)}$ the N the desired 'high quality' 3D images. We recall that each frame in $I_{HQ}^{(k)}$ is calculated by fusing several successive frames in I_{LQ} covering commmon informations. Practically, only successive frames contained in a sliding temporal window (centered on the working frame) were taken into account (let $\Delta T \geqslant 2$ be the size of this temporal window). We denote by $\rho \in [0,1]$ the ratio between the temporal window size and the total amount of frame N (we have $\rho = \frac{\Delta T}{N}$). We underline that ρ is a crucial user-defined parameter for the algorithm, and its impact on the overall results will be carrefully evaluated and discussed later.

An IBP algorithm (Irani and Peleg 1993) was employed in each 3D frame invidually in order to compensate for inherent numerical approximations arising from the application of 3D spatial transformations on images. We denote by $I_{HQ}^{(n)}\Big|_i$ the unnoisy guess (frame n) obtained at iteration i.

(i) An initial guess of the desired unnoisy image was first computed. For each frame $n \in [1,...,N]$, we computed the mean of noisy images contained in the above-mentioned temporal window (i.e. $I_{LQ}^{(k)}$, $\forall k \in \left[n - \frac{\Delta T}{2}, n + \frac{\Delta T}{2}\right[$), each image being registered onto the current position:

$$I_{HQ}^{(n)}\Big|_0 = \frac{1}{\Delta T} \sum_{k \in \left[n - \frac{\Delta T}{2}, n + \frac{\Delta T}{2}\right[} T_{n,k}\left(I_{LQ}^{(k)}\right). \tag{1}$$

The theoretical SNR improvement is analysed in appendix.

(ii) Noisy images $I_{LQ}^{(k)}\Big|_{i+1}$ ($k \in \left[n - \frac{\Delta T}{2}, n + \frac{\Delta T}{2}\right[$) which would be acquired if the guess was correct could then be estimated. To this end, the current guess of the unnoisy image $I_{HQ}^{(n)}\Big|_i$ was back-registered on each frame position using the 3D spatial deformations $T_{n,k}^{-1}$:

$$I_{LQ}^{(k)}\Big|_{i+1} = T_{n,k}^{-1}\left(I_{HQ}^{(n)}\Big|_i\right). \tag{2}$$

(iii) For each frame, the voxelwise differences between original and generated 3D noisy images could be calculated as follows:

$$\Sigma^{(n)} = \frac{1}{\Delta T} \sum_{k \in \left[n - \frac{\Delta T}{2}, n + \frac{\Delta T}{2}\right[} T_{n,k}\left(I_{LQ}^{(k)}\Big|_0 - I_{LQ}^{(k)}\Big|_{i+1}\right). \tag{3}$$

(iv) From a fixed-point scheme mimizing $\Sigma^{(n)}$, an updated unnoisy guess $I_{HQ}^{(n)}\Big|_{i+1}$ could be generated $\forall n \in \{1,...,N\}$:

$$I_{HQ}^{(n)}\Big|_{i+1} = I_{HQ}^{(n)}\Big|_i + \Sigma^{(n)}. \tag{4}$$

(v) The iterative process (ii)–(iv) was repeated ($I_{HQ}^{(n)}\Big|_i \rightarrow I_{HQ}^{(n)}$) until the relative variation of the residual error (i.e. the mean squared of $\Sigma^{(n)}$) fell below a pre-defined user threshold (noted ε). While a reduced value for ε may lead to an advantageous decrease of the residual error, it must also be high enough to prevent the algorithm to get caught in an infinite loop (for numerical precision considerations). In all presented experiments, a good compromise for $\varepsilon =$ has been found for a common value of 10%.

Note that, for the completion of all frames, the total number of forward/backward transformation pairs ($T_{n,k}$, $T_{n,k}^{-1}$) involved in equations (1)–(3) reached $\frac{N \times (N-1)}{2}$ using a temporal window size $\Delta T = N$. For computation time considerations, only needful pairs of transformations were pre-calculated in Step #2 and stored in random access memory (RAM) for fast access.

2.2. Experimental validation

Both the precision and the accuracy of the 4D outputs were quantitatively evaluated on the abdomen of 6 mice under free-breathing. The performance of the method was subsequently analysed on the heart of one mouse.

2.2.1. Experimental setup

Experiments were performed on a 7T Bruker Biospec system (Ettlingen, Germany), using a 4-phased array coil in a volume configuration (19 × 25.5 mm diameter, Rapid Biomedical). Acquisitions were performed on a group

of healthy mice (C57BL/6, body weights = 19–25 g, Charles River, France). All experimental procedures were approved by the Animal Care and Use Institutional ethics committee of Bordeaux, France (approval no. 5012032-A). The respiration was monitored using a balloon placed on the mouse abdomen. Respiratory rhythm was stabilized at 100 inspirations per minute and anesthesia was regulated by modifying the proportion of isoflurane inhaled. Before mouse positioning facing up in the magnet, 100 μmol Fe/kg of ultrasmall superparamagnetic iron oxide particles (Ferumoxytol, AMAG Pharmaceuticals) was injected through the tail vein to decrease the blood T1 longitudinal relaxation time and obtain a high blood signal.

2.2.2. MR protocol

A radial 3D self-gated UTE sequence (Cardiet *et al* 2019) was used to perform the acquisitions with the following parameters: Repetition time/Echo time (TR/TE) = 3.5/0.081 ms, excitation pulse/duration/angle = bloc pulse/0.05 ms/15°, field-of-view = 22.5 × 22.5 × 22.5 mm^3, matrix = 128 × 128 × 128, resulting in an isotropic voxel size of 176 μm, receiver bandwidth = 100 kHz. The number of samples per projection is equal to 75: 64 (matrix size) + 6 (ramp compensation) + 5 (Self-Gating samples). The radial acquisition scheme corresponding to 30 000 projections was repeated 40 times (with the number of repetitions noted NR) corresponding to a total acquisition duration of 70 min.

The self-gating signal, as already described in Hoerr *et al* (2013) and Trotier *et al* (2016), enables to identify respiratory and cardiac cycles. With the same data, cardiac or respiratory cine frames can be reconstructed. To do this, the k-space data were attributed, retrospectively, to the corresponding cine frame, according to their temporal position within the respiratory or cardiac cycle in order to generate 40 frames per breathing cycle or 30 frames per cardiac cycle.

To reconstruct the undersampled images, the 35 first minutes (NR = 20) and the 17 first minutes (NR = 10) and the 8 first minutes (NR = 5) of the acquired data were used.

2.2.3. Performance assessment in the thorax of 6 mice

Spatial analysis

All data acquired during the stable phase of the respiration cycle (from the 70 min acquisition time image, NR = 40) were summed retrospectively in order to produce a gold-standard high resolution 3D image. Then, the performance of the proposed approach could be assessed by evaluating the peak-SNR (pSNR) between the 3D enhanced output obtained at the stable phase of the exhalation and the gold-standard. For this purpose, for images with normalised intensity (values in the range $[0, 1]$), the pSNR can be obtained as follows:

$$\mathrm{pSNR} = 10 \times \log\left(\frac{1}{\mathrm{EQM}}\right). \tag{5}$$

EQM being the mean quadratic error between our output and the goldstandard, obtained after image registration (using an algorithm which aims at maximizing edge alignment between the images being registered (Denis de Senneville *et al* 2016), in order to prevent any impact on the EQM) and intensity standardization (Nyul and Udupa 1999) (an histogram matching of order 2 was employed (Christensen 2003)).

Temporal analysis

A signal intensity drop was observable in the lung at the end of the inhalation, presumably caused by the variation of proton density per voxels along breathing. The accuracy over time was evaluated by analysing time-intensity curves (TIC) calculated over a cubic region of 15 × 15 × 15 voxels (noted Γ) located in the lung. The TIC, applied on a given 4D image I, can be calculated as follows:

$$f_{I,\Gamma}(n) = \frac{1}{|\Gamma|}\sum_{\vec{r}\in\Gamma} I_{HQ}^{(n)}(\vec{r}) \tag{6}$$

$\vec{r} \in \Omega$ being the spatial location, Ω the image coordinates domain, n the time index, and $|\Gamma|$ the number of voxels in Γ ($|\Gamma| = 15^3$ in the current study).

The signal bias could then be evaluated by computing the mean absolute error (MAE) between TICs resulting from original ($f_{I_{LQ},\Gamma}(n)$) and enhanced ($f_{I_{HQ},\Gamma}(n)$) data-sets, over the N frames of the observed physiological cycle, as follows:

$$\mathrm{MAE} = \frac{1}{N}\sum_{n=1}^{N}\left|f_{I_{LQ},\Gamma}(n) - f_{I_{HQ},\Gamma}(n)\right|. \tag{7}$$

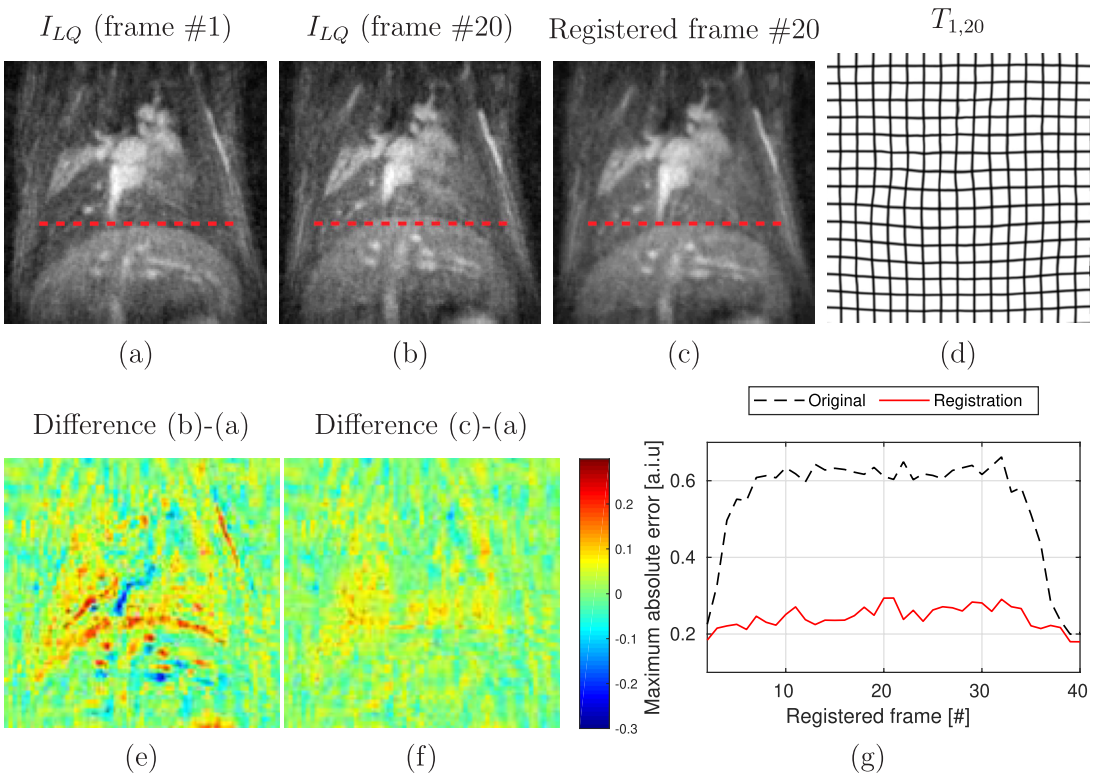

Figure 2. Typical registration results obtained using the implemented OF-algorithm (Step #2, see section 2.1.2) on the thorax of a mouse (acquisition duration = 35 min). The original input noisy images obtained at the begining (a) and at the end of the exhalation (b) are reported. (c) shows the image in (b) registered on position in (a) using the implemented optical-flow algorithm. Note that the displacement in the liver/lung interface can be observable thanks to the red dashed lines in ((a)–(c)). The estimated spatial deformation field is reported in (d). The voxelwise image difference obtained before (e) and after image registration (f) are reported. The maximum absolute difference is reported in (g) for each of the 40 frames before (black dashed plot) and after (red plot) image registration. (a) I_{LQ} (frame #1). (b) I_{LQ} (frame #20). (c) Registered frame #20. (d) $T_{1,20}$. (e) Difference (c)–(a). (f) Difference (b)–(a).

Comparison with compressed sensing techniques

Two compressed sensing strategies (referred to as 'CS-[1-2]') were analysed:

(i) **CS-1:** each 3D frame in the time sequence was individually reconstructed using a L_1-Wavelet regularization.
(ii) **CS-2:** the complete 4D data set was reconstructed using a L_1-Wavelet regularization for both spatial and temporal dimensions.

Compressed sensing reconstructions were performed using the Berkeley Advanced Reconstruction Toolbox (BART, DOI: https://doi.org/10.5281/zenodo.592960). The estimation of the coil sensitivity was performed using the ESPIRiT calibration approach (Uecker *et al* 2014). A manual tuning of regularization parameters was performed and only best achievable results are reported in this study.

Statistical analysis

A Wilcoxon paired test was carried out in order to study whether pSNR and MAE differences are statistically significant between original, Compressed sensing and IBP-enhanced data sets, and between all pairs of tested ρ values. A significance threshold of $p = 0.05$ was used.

2.2.4. *Performance assessment in the heart of a mouse*

A qualitative analysis was performed as follows: we first observed mis-registered areas by analysing image difference between the images being registered. Subsequently, intensity biases on enhanced images were analysed on voxelwise difference maps calculated between original and enhanced images.

Note that the use of a goldstandard image was hardly feasible in the heart (insufficient steady periods were present in the cardiac motion pattern), preventing pSNR calculations in the scope of this experiment.

2.2.5. *Benchmark*

Above-mentioned performance indicators were evaluated for acquisition durations of 8, 17 and 35 min and for ρ values of 5%, 20% and 100%.

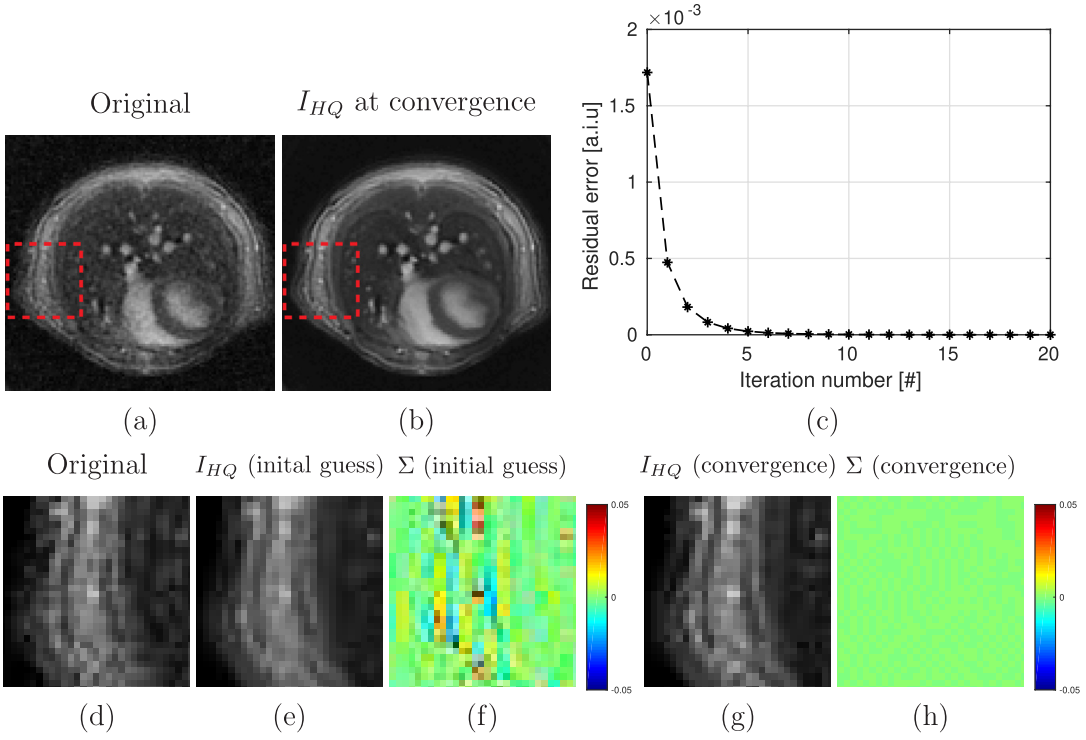

Figure 3. Typical example of the IBP-enhancement (Step #3, see section 2.1.3) of an image acquired on the abdomen of a mouse during the stable phase of the exhalation. (a) original image (acquisition duration = 35 min, $\rho = 100\%$), (b) IBP-enhanced image at convergence, (c) residual error as a function of the iteration number. The original image (d), the initial guess (e) and its corresponding residual error map at (f), the guess at convergence (g) and its corresponding residual error map (h) are emphasized within a region of interest delimited by the red dashed rectangles in ((a) and (b)). Note that units in ((c), (f) and (h)) are arbitrary intensity units (a.i.u). (a) Original. (b) I_{HQ} at convergence. (d) Original. (e) I_{HQ} (inital guess). (f) Σ (initial guess). (g) I_{HQ} (convergence). (h) Σ (convergence).

Note that, for the thorax experiment, ρ values of 5%, 20% and 100% corresponded to temporal sliding windows sizes ΔT of 2, 8 and 40 frames, respectively. For the heart experiment, it corresponded to $\Delta T = 2, 6$ and 30 frames, respectively.

2.2.6. Hardware and implementation

We evaluated the computational overhead of our method using two different hardware architectures:

Test platform #1

This platform employed commodity CPU/GPU hardwares. An Intel 2.5 GHz i7 workstation (Quad-core) with 32 GB of RAM was used. The GPU was a NVidia GeForce GTX 770 with 2 GB of dynamic random-access memory (NVIDIA, Santa Clara, CA, USA). We separately tested three hardware configurations: (i) OF-registration tasks were performed by the CPU only (each individual OF-registration being multi-threaded on the four available CPU); (ii) registration tasks were performed by the GPU only; (iii) OF-registration tasks were split into two groups, each group being respectively tackled simultaneously by the CPU and the GPU (the size of each group was optimized for an optimal hardware utilisation).

Test platform #2

This platform was a computer cluster with 9 nodes of Intel Xeon E5-2680 2.5 GHz (2 Dodeca-core) with 128 GB of RAM.

The implementation was performed in C++ and parallelized through multi-threading. The GPU implementation was realized using the compute unified device architecture (CUDA) (NVIDIA 2008).

3. Results

3.1. Performance assessment in the thorax of 6 mice

A visualization of typical OF-registration results obtained in the thorax of a mouse is reported in figure 2. The implemented OF-algorithm estimated a spatially regular elastic deformation (mainly head-foot, as expected), as shown in figure 2(d). The maximum absolute difference between the reference and the registered image

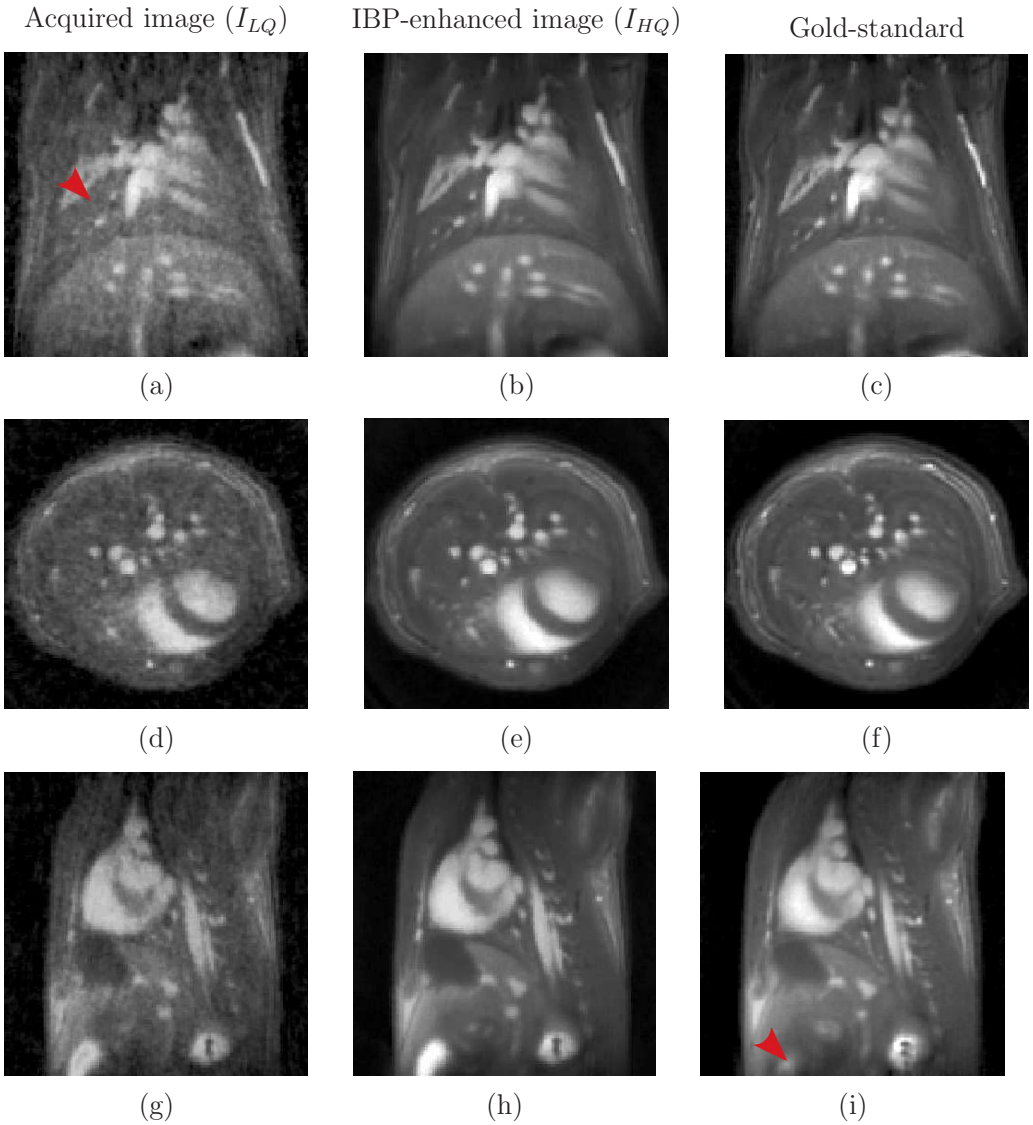

Figure 4. Typical results obtained on the thorax of a mouse during the stable phase of the exhalation. The original (left column, acquisition duration = 17 min), the corresponding IBP-enhanced (center column, $\rho = 100\%$) and the goldstandard images (right column) are shown. Coronal, transversal and sagittal images are displayed in the 1st, 2nd and 3rd lines, respectively.

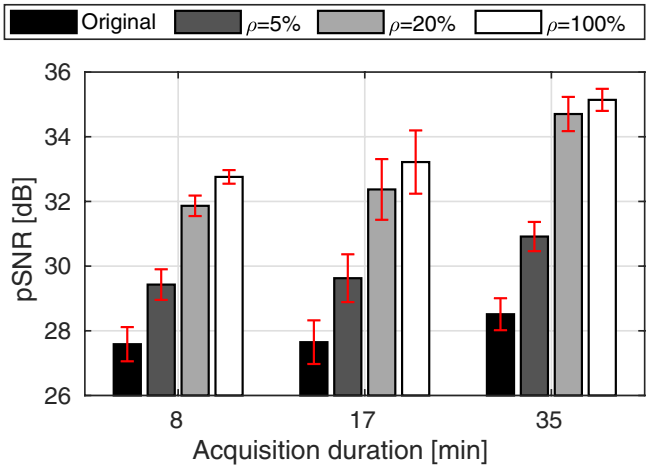

Figure 5. Summary of pSNR values obtained for various acquisition durations (8, 17 and 35 min) and ρ values of 5%, 20% and 100%. Standard deviations over the 6 mice are given by the size of the red error bars.

Table 1. Summary of pSNR and MAE numerical values obtained for various acquisition durations (8, 17 and 35 min) and all tested reconstruction methods.

	Experiment					
	8 min		17 min		35 min	
Reconstruction	pSNR	MAE ($\times 10^{-4}$)	pSNR	MAE ($\times 10^{-4}$)	pSNR	MAE ($\times 10^{-4}$)
Original	27.3 ± 1.1	0 ± 0	27.4 ± 1.3	0 ± 0	28.3 ± 1	0 ± 0
IBP [$\rho = 5\%$]	29 ± 1	34 ± 7	29.3 ± 1.5	34 ± 15	30.7 ± 0.9	25 ± 5
IBP [$\rho = 20\%$]	31.3 ± 0.9	47 ± 14	31.9 ± 1.8	47 ± 19	34.3 ± 1.1	37 ± 14
IBP [$\rho = 100\%$]	32 ± 0.7	199 ± 45	32.6 ± 1.9	195 ± 43	34.7 ± 0.6	194 ± 41
CS-1	28.4 ± 1.4	40 ± 14	28.8 ± 1.1	42 ± 9	29.5 ± 1.1	49 ± 8
CS-2	29.7 ± 1.4	49 ± 14	29.6 ± 1	49 ± 9	29.8 ± 1	53 ± 6

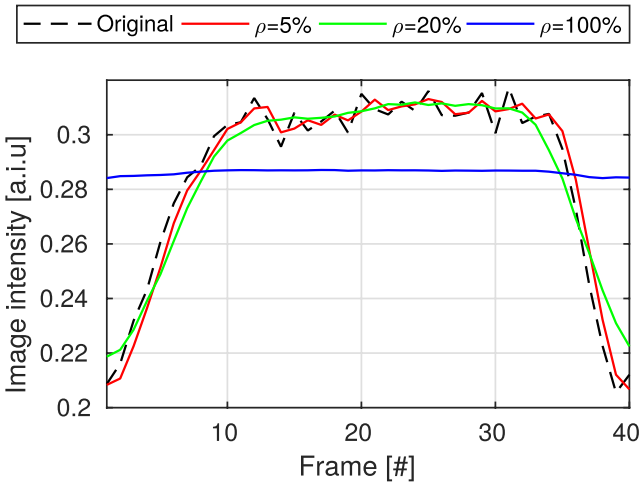

Figure 6. Time intensity curves obtained in a region of $15 \times 15 \times 15$ voxels located in the lung a mouse (red arrow in figure 4(a)) for ρ values of 5%, 20% and 100%.

decreased by 60% when the OF-based registration was applied (figure 2(f)), even for two images associated to opposite instants of the breathing cycle (i.e. $I_{LQ}^{(1)}\big|_0$ and $I_{LQ}^{(20)}\big|_0$). This maximum absolute difference remained almost constant throughout the complete breathing cycle and did not exceed the basal level (see figure 2(g)), demonstrating steady performance of the employed OF algorithm.

The image quality visually improved with an increasing iteration number in the IBP algorithm, as shown in figures 3(d), (e) and (g). The corresponding voxelwise error decreased accordingly (see figures 3(f) and (h)). The residual error, as a function of the iteration number, depicted a strict decrease toward zero (figure 3(c)) showing the convergence of the implemented fixed point scheme (equation (4)). At convergence, figure 4 shows that the enhanced image obtained at the end of the exhalation (figures 4(b), (e) and (h)) was visually more similar to the gold-standard (figures 4(c), (f) and (i)) as compared to the original one (figures 4(a), (d) and (g)). Videos of typical IBP-enhanced 4D images (acquisition duration = 8 min, $\rho = 100\%$) are provided in supplemental data (stacks.iop.org/PMB/65/015003/mmedia). This visual inspection is confirmed in figure 5 and table 1 for all tested mice. Only the following test did not shown statistically significantly different pSNR values: (35 min/$\rho = 20\%$) versus (35 min/$\rho = 100\%$) ($p = 0.16$). For all other scenarios, the pSNR significantly increased for increased ρ value, for all tested acquisition durations ($p < 0.03$). Using the proposed approach, an acquisition duration of 8 min led to a pSNR higher than the one obtained on the original image with an acquisition duration of 35 min. Figures 6 and 7 provide a temporal analysis of the data. The signal in the lung drop during the exhalation, as shown by the black dashed line in figure 6. Although the time intensity curve obtained for $\rho = 5\%$ visually fitted nicely this trend (red line), this were not the case at the end of inhalation for $\rho = 20\%$ (green line), and even worse for $\rho = 100\%$ (black line. No temporal variation was screened here). These observations are confirmed for all tested mice and acquisition durations in figure 7. The proposed IBP approach is compared with several up-to-date compressed sensing strategies in figure 8. It can be observed that both pSNR (figures 8(e)) and MAE (figure 8(f)) values were better using combined the spatio-temporal regularization strategy (CS-2) as compared to the frame-by-frame based strategy (CS-1). One can notice that, by setting $\rho = 20\%$, a significantly higher pSNR was

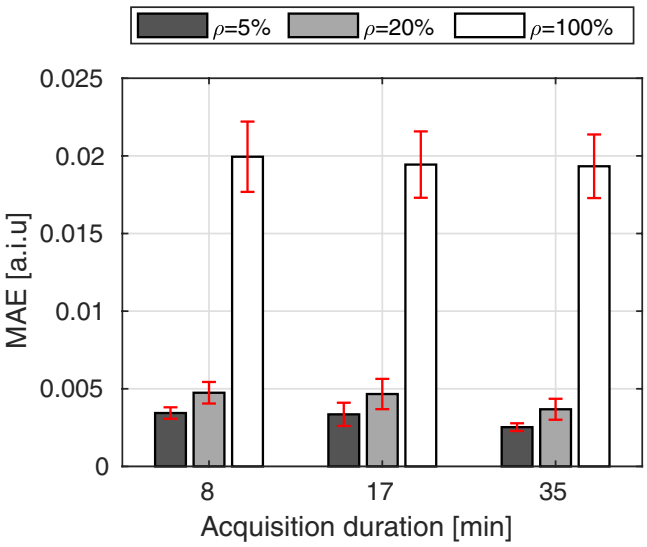

Figure 7. Summary of MAE (as defined in equation (7)) obtained for various acquisition durations (8, 17 and 35 min) and ρ values of 5%, 20% and 100%). Standard deviations over the 6 mice are given by the size of the red error bars.

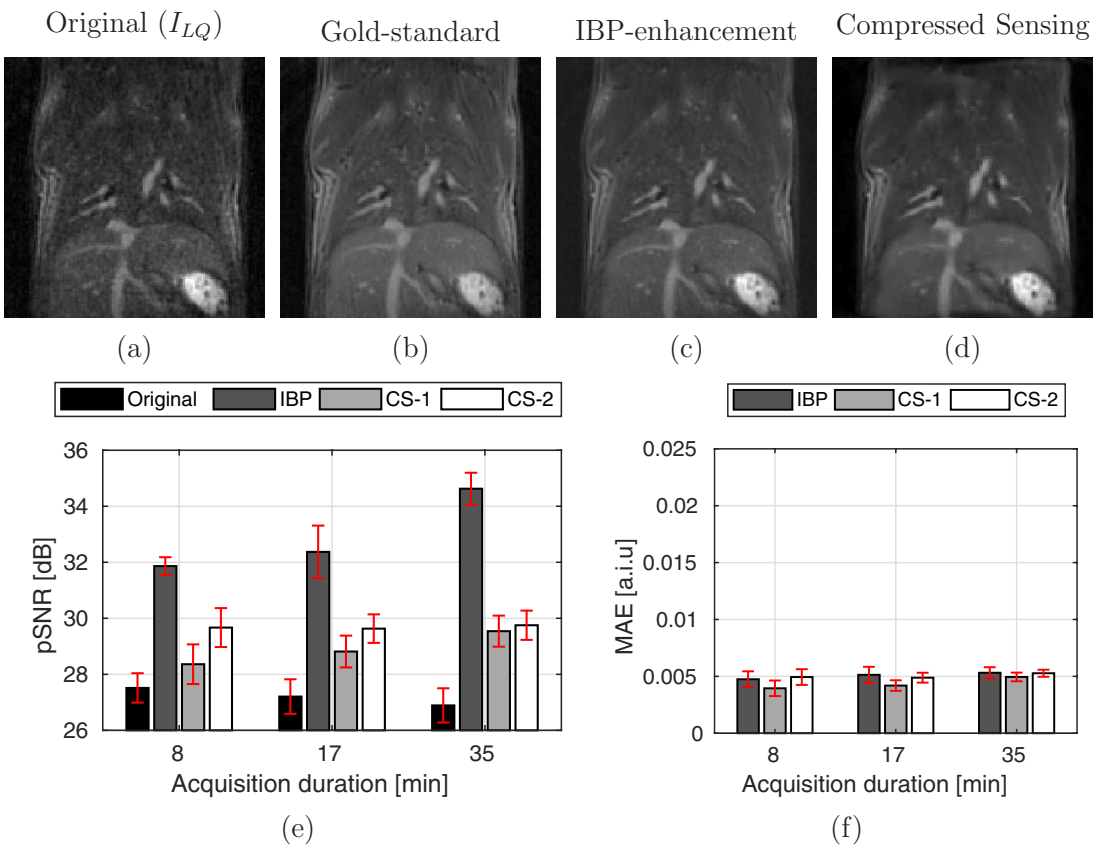

Figure 8. Typical results obtained using IBP and compressed sensing approaches. (a) Original image (acquisition duration = 8 min), (b) gold-standard image, (c) IBP-enhanced image ($\rho = 20\%$), (d) compressed sensing reconstruction (CS-2). pSNR and MAE values are summarized for each tested reconstruction methods (original, IBP with $\rho = 20\%$ and compressed sensing values) for various acquisition durations (8, 17 and 35 min) in (e) and (f), respectively. Standard deviations over the 6 mice are given by the size of the red error bars. (a) Original (I_{LQ}). (b) Gold-standard. (c) IBP-enhancement. (d) Compressed sensing.

obtained using the proposed IBP approach ($p < 0.03$), as compared to CS-1 and CS-2, together with a similar MAE penalty ($p > 0.3$).

3.2. Performance assessment in the heart of a mouse

A visualization of typical OF-registration results obtained in the heart of a mouse is reported in figure 9. The implemented OF-algorithm estimated a complex local deformation, as shown in figure 9(d). The maximum

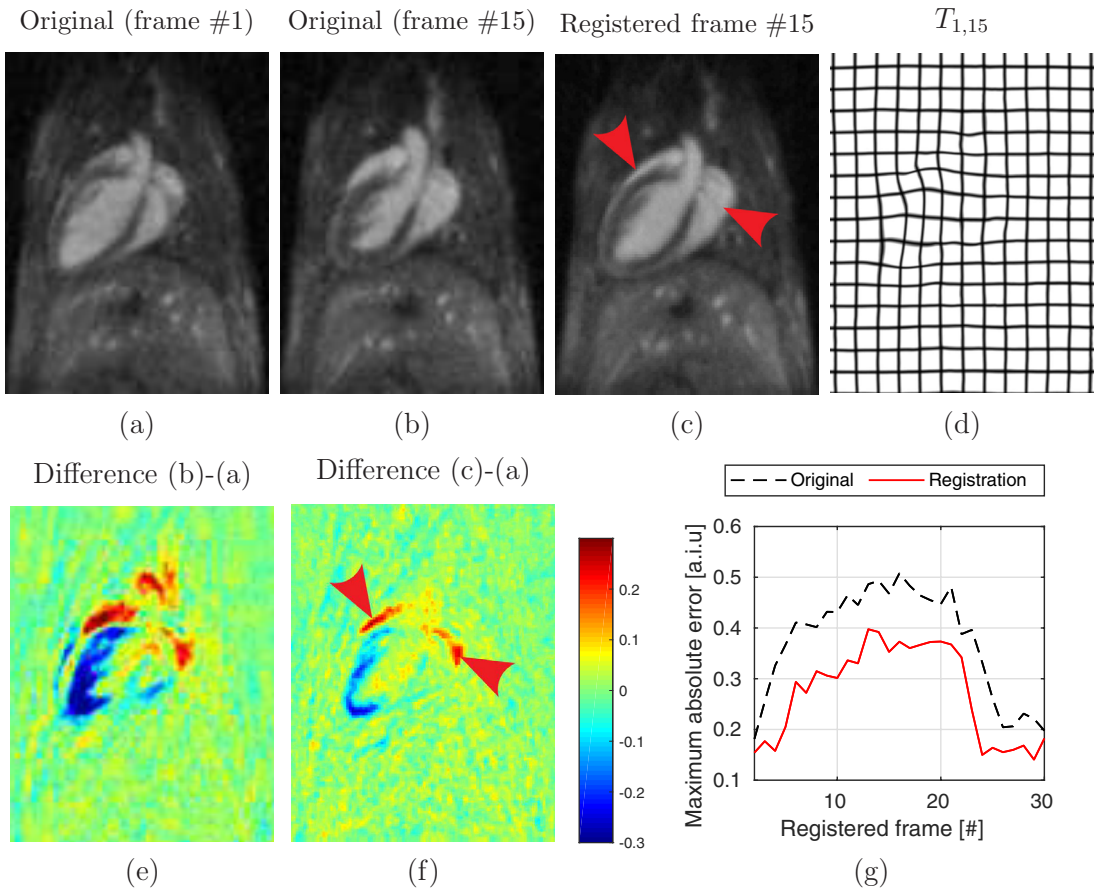

Figure 9. Typical registration results obtained using the implemented OF-algorithm (see section 2.1.2) on the heart of a mouse. The original input noisy images are reported for two different instants of the cardiac cycle in (a) and (b). (c) Shows the image in (b) registered on position in (a) using the implemented OF algorithm.The estimated spatial deformation field is reported in (d). The voxelwise image difference obtained before (e) and after image registration (f) are reported. Note that high values in (f) are obtained in mis-registered areas (see red arrows in (c) and (f)). The maximum absolute difference is reported in (g) for the individual registration of all acquired frames onto the image in (a) before (black dashed plot) and after (red plot) image registration. (a) Original (frame #1). (b) Original (frame #15). (c) Registered frame #15. (d) $T_{1,15}$. (e) Difference (b)–(a). (f) Difference (c)–(a).

absolute difference between the reference (reported in figure 9(a)) and the registered image (reported in figure 9(b)) decreased by only 20% when the OF-based registration was applied (figure 9(f)). The maximum absolute difference increased during the cardiac cycle, even approaching the values obtained when no registration was applied, demonstrating poor performance of the employed OF algorithm for images prone to complex deformations.

Figure 10 displays the performance of IBP-enhancement for ρ values of 5%, 20% and 100%. For ρ values of 5% and 20%, voxelwise image differences between original and IBP-enhanced images shown comparable values in the heart and in the surrounding tissues (see figures 10(e) and (f)). This was however not the case for $\rho = 100\%$: large image differences are observable in figure 10(g), especially in areas pointed by red arrows. Note that these regions match nicely mis-registered areas (see red arrows in figures 9(c) and (f)).

3.3. Computational request

A computational benchmark of our implementations of the proposed reconstruction strategy, obtained for different ρ values using our two test platforms, is provided in table 2. As expected, the computation time greatly benefited from our combined CPU/GPU implementation, and huge speed-up could be obtained using the computer cluster. About 15 min were necessary to enhance 40 frames of $128 \times 128 \times 128$ voxels (the thorax MR-scan) with $\rho = 5\%$ using our commodity hardware. A computer cluster complete the same task within less than a minute. While around one hour was needed using our commodity hardware for $\rho = 100\%$, three minutes only were mandatory using our computer cluster.

4. Discussion

The strategy consists of privileging spatial resolution/frame number of the acquired MR-data as well as isotropic voxel sizes and large FOV, the consequential SNR penalty being adressed using an IBP approach. The benefit of

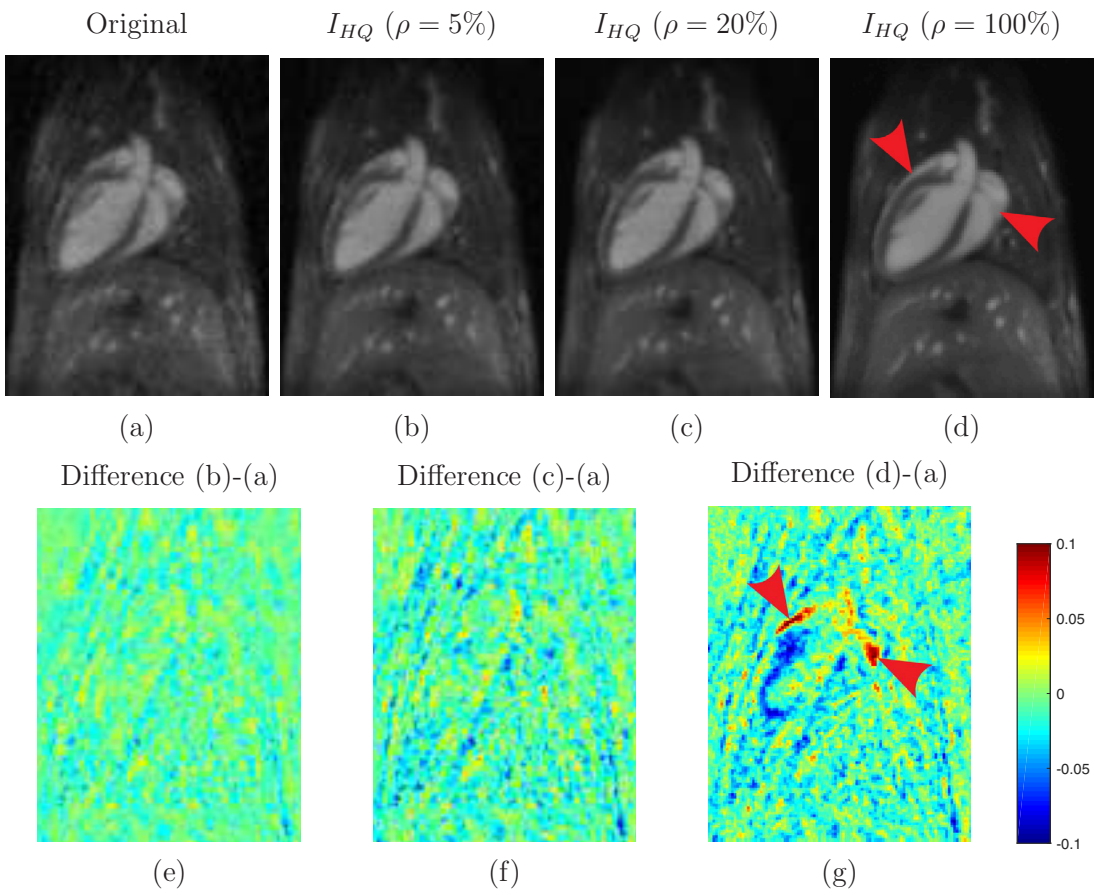

Figure 10. IBP-enhanced image of the heart of a mouse. The original (a) and the IBP-enhanced images obtained for ρ values of 5% (b), 20% (c) and 100% (d) are shown. The voxelwise image difference between the original image and the IBP-enhanced images obtained for ρ values of 5% (e), 20% (f) and 100% (g) are reported. (a) Original. (b) I_{HQ} ($\rho = 5\%$). (c) I_{HQ} ($\rho = 20\%$). (d) I_{HQ} ($\rho = 100\%$). (e) Difference (b)–(a). (f) Difference (c)–(a). (g) Difference (d)–(a).

the increased frame number is two-fold: first, reduced scan times allows limiting intra-scan motion artifacts. Second, the temporal resolution is converted into SNR thanks to the IBP strategy.

The proposed IBP approach acts like an 'improved' temporal filter in the sense that it is able to compensate for spatial organ deformations, and ensuing interpolation biases. The input parameter ρ controls the kernel size (ΔT) of this average filter and, by the way, its cut-of-frequency. ρ thereby allows adjusting the balance between the precision gain and the inherent resulting penalty on the output accuracy. Practically, the algorithm is prone to catch high temporal frequencies of the signal for low ρ values (see red curve in figure 6). Conversely, any temporal signal variations not attributed to motion may be dropped for $\rho = 100\%$ (see blue curve in figure 6).

In theory, the overall precision gain (i.e the noise standard deviation reduction) is equal to $\sqrt{\Delta T}$ (see appendix). In return for the above-mentioned precision benefit, a penalty factor of ΔT is applied on the temporal resolution of signal variations not attributed to motion. On the thorax experiments, it is interesting to note that a moderate ρ value of 5% (which corresponded to a temporal window of 2 frames) improved greatly the pSNR (by $\simeq$2 dB, which matched the theoretical SNR improvement ratio of $\sqrt{2}$ arising from equation (A.1)): this rendered the pSNR obtained using an acquisition duration of 8 min greater than the one obtained using an acquisition duration of 35 min without IBP-enhancement (see figure 5). This was achievable together with a moderate impact on the output accuracy: a penalty factor of 2 was applied on temporal signal variations not attributed to motion (see the red curve in figure 6).

The input parameter ρ has thus to be chosen according to the final practical application: for segmentation/delineation propagation tasks, a high ρ value may be beneficial in order to enhance anatomical contrasts whatever the gray intensities of these latter. For processings based on a quantitative image contrast analysis, low ρ value may be preferable in order to prevent inherent reconstruction biases on overall results.

The performance of the reconstruction also rely on the ability of the employed image registration algorithm to catch organ deformations. We chose a 3D OF algorithm, because of its short processing time and minimal user intervention. The implemented OF algorithm shown steady efficiency throughout the complete breathing cycle in the thorax experiment (see figure 2), allowing the use large temporal window sizes (see figures 5 and 7). Low

Table 2. Computation time (in minutes) obtained using our implementation (OF-calculations + IBP algorithm) on our two test platforms, for the thorax and heart experiments, for different ρ values.

		Computation time (min)			
		Test platform #1			Test platform #2
Experiment		4-CPU	GPU	4-CPU/GPU	9-Nodes of 24-CPU
Thorax	$\rho = 5\%$	34	28	15	1
	$\rho = 20\%$	69	46	31	2
	$\rho = 100\%$	145	117	65	3
Heart	$\rho = 5\%$	25	20	11	1
	$\rho = 20\%$	41	34	19	1
	$\rho = 100\%$	81	68	37	2

ρ value ($\leqslant 20\%$) were however mandatory for the heart experiment in order reduce the complexity of spatial deformations within the used temporal window (see figures 9 and 10). It must be however underlined that there is no easy approach to establish the robustness of OF-estimates without having any sort of silver or gold standard. We believe that the use of quality assurance criteria (QA) on motion estimates (Zachiu *et al* 2018) is a promising path of investigation.

It must be reported that the use of a goldstandard image for pSNR evaluation has several inherent limitations. We recall that sufficient steady periods needed to be present in the motion pattern in order to increase the amount of data in the k-space while avoiding intra-scan motion artifacts. In the thorax experiments, only data acquired at the end of the exhalation could be used. However, quite lenghty acquisition (70 min) were mandatory and peristaltic/motion drifts were likely to occur (see red arrow in figure 4(i)). These latter may not be present in the used input data sets, which hampered in turns our pSNR evaluation.

While existing motion correction strategies operating in the k-space are inherently restrained to translational and rotational movements, the proposed approach, which operates in the spatial domain, allows accumulating signal with complex elastic organ deformations. We expect that motion correction strategies in the k-space may be beneficial to reduce intra-scans artifacts of our input images and, in turn, to further improve our output quality.

Most of computation time are devoted to the completion of needed OF-calculations. Using the proposed technique, OF-calculations can be performed individually for different frame pairs. That way, the computation time greatly benefits from a combined CPU/GPU (test platform #1) or computer cluster architectures (test platform #2).

5. Conclusion

The proposed method enriches the acquisition and reconstruction tasks by a subsequent IBP-enhancement step. Our results match theoretical expectations: a pSNR gain of 2 dB could be obtained with a moderate penalty factor 2 on the temporal resolution. In this context, the IBP-enhancement of a 4D-MRI acquired in 8 min led to a precision higher than the one acquired in 35 min. Up to 6 dB was also achievable by totally sacrificing the temporal resolution. The proposed implementation is easily parallelizable and takes great benefit of computer cluster architectures. The method was thus compatible with a clinically acceptable time duration: 8 and less than 3 min were successively mandatory for MR-acquisition and IBP-algorithm (including OF-calculations), respectively.

Future works will include the compensation of additional sources of artifacts (potential biases arising either from intra-scan movements or from the Rician noise distribution in MR-magnitude images which is a non-zero mean distribution), the developement of an improved motion estimation model, the IBP-enhancement of MR-T_1, -T_2 and -T_2^* images as well as the evaluation of the method on patients.

Acknowledgment

Experiments presented in this paper were carried out using the PlaFRIM experimental testbed, supported by Inria, CNRS (LABRI and IMB), Université de Bordeaux, Bordeaux INP and Conseil Régional d'Aquitaine (see www.plafrim.fr/). The authors thank the Laboratory of Excellence TRAIL ANR-10-LABX-57 for funding. This study has been carried out with the financial support of the French National Research Agency (ANR) in the frame of the 'Investments for the future' Programme IdEx Bordeaux-CPU (ANR-10-IDEX-03-02).

Appendix. Theoretical analysis of noise reduction

A temporal data averaging is performed in equation (1). Let $\sigma(I_{LQ})$ be the noise standard deviation in $T_{n,k}\left(I_{LQ}^{(k)}\right)$, assuming an identically distributed noise $\forall k \in \{1, ..., N\}$. It quickly comes that the noise standard deviation of $I_{HQ}^{(n)}\Big|_0$ is theoretically equal to:

$$\sigma\left(I_{HQ}^{(n)}\Big|_0\right) = \frac{1}{\sqrt{\Delta T}}\sigma\left(I_{LQ}\right). \tag{A.1}$$

Equation (1) thus enabled a theoretical SNR reduction by $\sqrt{\Delta T}$.

References

Cardiet C, Trotier A, Ribot E, Denis de Senneville B and Miraux S 2019 Self-gated 5D cardiac MRI in mice: a detailed study *ISMRM Proc. 27th Annual Meeting ISMRM* vol 1080

Chen F, Zhang T, Cheng J Y, Shi X, Pauly J M and Vasanawala S S 2017 Autocalibrating motion-corrected wave-encoding for highly accelerated free-breathing abdominal MRI *Magn. Reson. Med.* **78** 1757–66

Cheng J Y, Alley M T, Cunningham C H, Vasanawala S S, Pauly J M and Lustig M 2012 Nonrigid motion correction in 3D using autofocusing with localized linear translations *Magn. Reson. Med.* **68** 1785–97

Cheng J Y, Zhang T, Ruangwattanapaisarn N, Alley M T, Uecker M, Pauly J M, Lustig M and Vasanawala S S 2015 Free-breathing pediatric mri with nonrigid motion correction and acceleration *J. Magn. Reson. Imaging* **42** 407–20

Chilla G S V N, Tan C H and Poh C L 2017 Deformable registration-based super-resolution for isotropic reconstruction of 4D MRI volumes *IEEE J. Biomed. Health Inform.* **21** 1617–24

Christensen G and Johnson H 2001 Consistent image registration *IEEE Trans. Med. Imaging* **20** 568–82

Christensen J D 2003 Normalization of brain magnetic resonance images using histogram even-order derivative analysis *Magn. Reson. Imaging* **21** 817–20

Denis de Senneville B, Zachiu C, Ries M and Moonen C T W 2016 Evolution: an edge-based variational method for non-rigid multi-modal image registration *Phys. Med. Biol.* **61** 7377

Dournes G, Menut F, Macey J, Fayon M, Chateil J F, Salel M, Corneloup O, Montaudon M, Berger P and Laurent F 2016 Lung morphology assessment of cystic fibrosis using MRI with ultra-short echo time at submillimeter spatial resolution *Eur. Radiol.* **26** 3811–20

Feng L, Coppo S, Piccini D, Yerly J, Lim R P, Masci P G, Stuber M, Sodickson D K and Otazo R 2018 5D whole-heart sparse MRI *Magn. Reson. Med.* **79** 826–38

Feng L *et al* 2019 Simultaneous evaluation of lung anatomy and ventilation using 4d respiratory-motion-resolved ultrashort echo time sparse mri *J. Magn. Reson. Imaging* **49** 411–22

Ferrer C J, Bos C, Denis de Senneville B, Borman P, Stemkens B, Tijssen R, Moonen C T W and Bartels L 2019 A planning strategy for combined motion-assisted/gated MR guided focused ultrasound treatment of the pancreas *Int. J. Hyperth.* **36** 702–11

Freedman J N, Collins D J, Gurney-Champion O J, McClelland J R, Nill S, Oelfke U, Leach M O and Wetscherek A 2018 Super-resolution t2-weighted 4D MRI for image guided radiotherapy *Radiother. Oncol.* **129** 486–93

Han F, Zhou Z, Cao M, Yang Y, Sheng K and Hu P 2017 Respiratory motion-resolved, self-gated 4D-MRI using rotating cartesian k-space (ROCK) *Med. Phys.* **44** 1359–68

Higano N S, Hahn A D, Tkach J A, Cao X, Walkup L L, Thomen R P, Merhar S L, Kingma P S, Fain S B and Woods J C 2017 Retrospective respiratory self-gating and removal of bulk motion in pulmonary UTE MRI of neonates and adults *Magn. Reson. Med.* **77** 1284–95

Hoerr V, Nagelmann N, Nauerth A, Kuhlmann M T, Stypmann J and Faber C 2013 Cardiac-respiratory self-gated cine ultra-short echo time (UTE) cardiovascular magnetic resonance for assessment of functional cardiac parameters at high magnetic fields *J. Cardiovascular Magn. Reson.* **15** 59

Irani M and Peleg S 1993 Motion analysis for image enhancement: resolution, occlusion, and transparency *J. Vis. Commun. Image Rep.* **4** 324–35

Jahnke C, Paetsch I, Gebker R, Bornstedt A, Fleck E and Nagel E 2006 Accelerated 4D dobutamine stress MR imaging with k-t BLAST: feasibility and diagnostic performance *Radiology* **241** 718–28

Jinsoo U, Matthew J K, Yimei L, Xingyu L, Christopher T, John T L, Thomas E M D and Hua C 2017 Quantification of pediatric abdominal organ motion with a 4D magnetic resonance imaging method *Int. J. Radiat. Oncol. Biol. Phys.* **99** 227–37

Liu Y, Yin F, Czito B G, Bashir M R and Cai J 2015 T2-weighted four dimensional magnetic resonance imaging with result-driven phase sorting *Med. Phys.* **42** 4460–71

NVIDIA 2008 NVIDIA CUDA: compute unified device architecture, programming guide, 2.0 edition (Santa Clara, CA: NVIDIA Corporation)

Nyul L G and Udupa J K 1999 On standardizing the MR image intensity scale *Magn. Reson. Med.* **42** 1072–81

Ohno Y, Koyama H, Yoshikawa T, Kishida Y, Seki S, Takenaka D, Yui M, Miyazaki M and Sugimura K 2017 Standard-, reduced-, and no-dose thin-section radiologic examinations: comparison of capability for nodule detection and nodule type assessment in patients suspected of having pulmonary nodules *Radiology* **284** 562–73

Paganelli C, Summers P, Bellomi M, Baroni G and Riboldi M 2015 Liver 4dmri: a retrospective image-based sorting method *Med. Phys.* **42** 4814–21

Stemkens B, Tijssen R, Denis de Senneville B, Heerkens H D, van Vulpen M, Lagendijk J and van den Berg C 2015 Optimizing 4D magnetic resonance imaging data sampling for respiratory motion analysis of pancreatic tumors *Int. J. Radiat. Oncol. Biol. Phys.* **91** 571–8

Stemkens B, Tijssen R H N, Denis de Senneville B, Lagendijk J J W and van den Berg C A T 2016 Image-driven, model-based 3d abdominal motion estimation for MR-guided radiotherapy *Phys. Med. Biol.* **61** 5335–55

Trotier A J, Castets C R, Lefranois W, Ribot E J, Franconi J M, Thiaudière E and Miraux S 2016 USPIO-enhanced 3D-cine self-gated cardiac MRI based on a stack-of-stars golden angle short echo time sequence: application on mice with acute myocardial infarction *J. Magn. Reson. Imaging* **44** 355–65

Tryggestad E, Flammang A, Han-Oh S, Hales R, Herman J, McNutt T, Roland T, Shea S M and Wong J 2013 Respiration-based sorting of dynamic MRI to derive representative 4D-MRI for radiotherapy planning *Med. Phys.* **40** 051909

Uecker M, Lai P, Murphy M J, Virtue P, Elad M, Pauly J M, Vasanawala S S and Lustig M 2014 ESPIRiTan eigenvalue approach to autocalibrating parallel MRI: where SENSE meets GRAPPA *Magn. Reson. Med.* **71** 990–1001

Van Reeth E, Tan C H, Tham I W and Poh C L 2015 Isotropic reconstruction of a 4D MRI thoracic sequence using super-resolution *Magn. Reson. Med.* **73** 784–93

Zachiu C, Denis de Senneville B, Moonen C T W, Raaymakers B W and Ries M 2018 Anatomically plausible models and quality assurance criteria for online mono- and multi-modal medical image registration *Phys. Med. Biol.* **63** 155016

Zachiu C, Papadakis N, Ries M, Moonen C T W and Denis de Senneville B 2015 An improved optical flow tracking technique for real-time MR-guided beam therapies in moving organs *Phys. Med. Biol.* **60** 9003

Zhang T, Cheng J Y, Potnick A G, Barth R A, Alley M T, Uecker M, Lustig M, Pauly J M and Vasanawala S S 2015 Fast pediatric 3D free-breathing abdominal dynamic contrast enhanced MRI with high spatiotemporal resolution *J. Magn. Reson. Imaging* **41** 460–73